Volume 6 | Number 11 | 7 June 2014 | Pages 5557–6188

Nanoscale

www.rsc.org/nanoscale

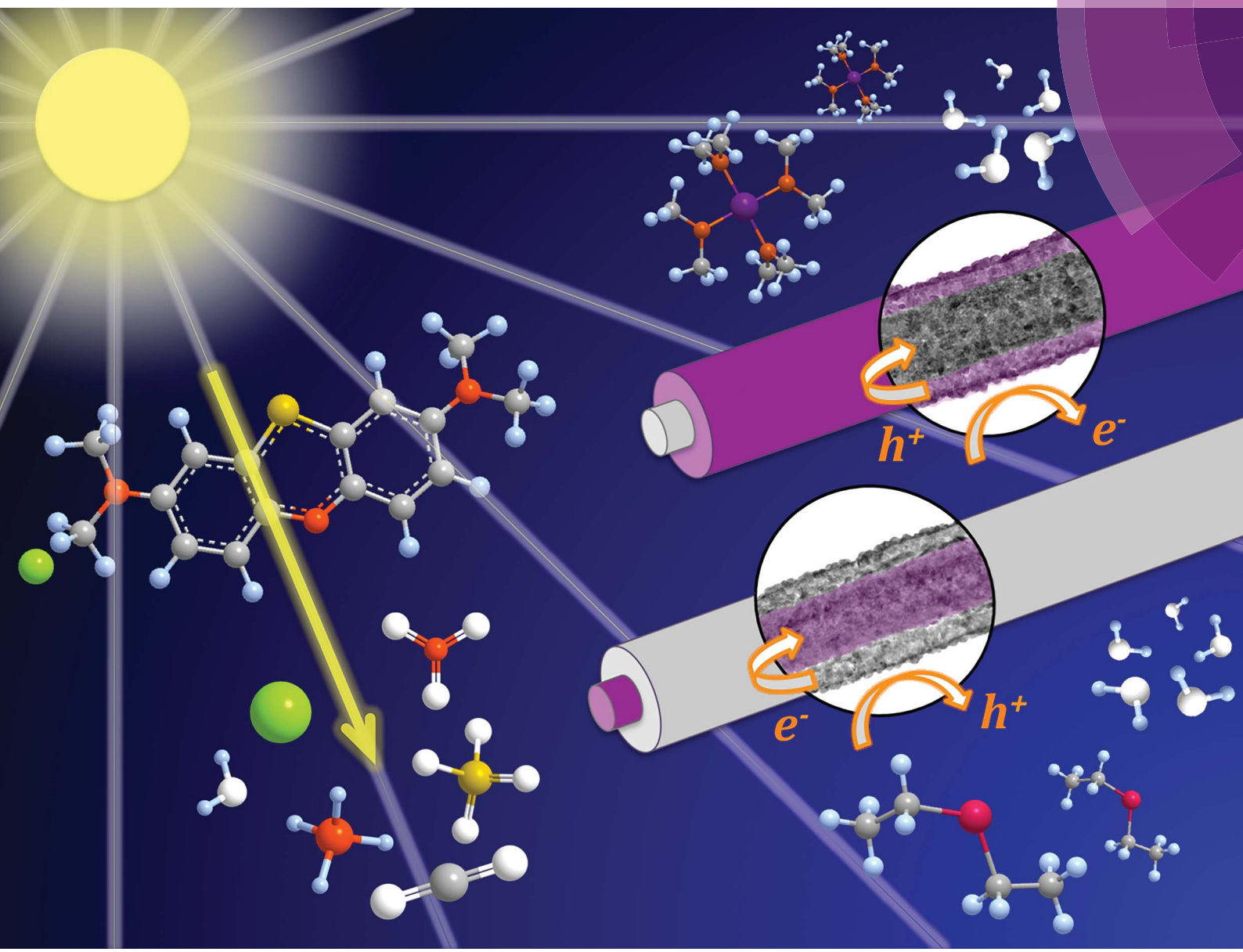

ISSN 2040-3364

ROYAL SOCIETY OF CHEMISTRY

PAPER

Sesha Vempati, Tamer Uyar *et al.*

Selective isolation of the *electron* or *hole* in photocatalysis: ZnO–TiO_2 and TiO_2–ZnO core–shell structured heterojunction nanofibers *via* electrospinning and atomic layer deposition

NCNST

Nanoscale

PAPER

View Article Online
View Journal | View Issue

Cite this: *Nanoscale*, 2014, **6**, 5735

Selective isolation of the *electron* or *hole* in photocatalysis: ZnO–TiO_2 and TiO_2–ZnO core–shell structured heterojunction nanofibers *via* electrospinning and atomic layer deposition†

Fatma Kayaci,[ab] Sesha Vempati,*[a] Cagla Ozgit-Akgun,[ab] Inci Donmez,[ab] Necmi Biyikli[ab] and Tamer Uyar*[ab]

Received 16th December 2013
Accepted 4th February 2014

DOI: 10.1039/c3nr06665g

www.rsc.org/nanoscale

Heterojunctions are a well-studied material combination in photocatalysis studies, the majority of which aim to improve the efficacy of the catalysts. Developing novel catalysts begs the question of which photo-generated charge carrier is more efficient in the process of catalysis and the associated mechanism. To address this issue we have fabricated core–shell heterojunction (CSHJ) nanofibers from ZnO and TiO_2 in two combinations where only the 'shell' part of the heterojunction is exposed to the environment to participate in the photocatalysis. Core and shell structures were fabricated *via* electrospinning and atomic layer deposition, respectively which were then subjected to calcination. These CSHJs were characterized and studied for photocatalytic activity (PCA). These two combinations expose *electrons* or *holes* selectively to the environment. Under suitable illumination of the ZnO–TiO_2 CSHJ, *e*/*h* pairs are created mainly in TiO_2 and the *electrons* take part in catalysis (*i.e.* reduce the organic dye) at the conduction band or oxygen vacancy sites of the 'shell', while *holes* migrate to the core of the structure. Conversely, *holes* take part in catalysis and *electrons* diffuse to the core in the case of a TiO_2–ZnO CSHJ. The results further revealed that the TiO_2–ZnO CSHJ shows ~1.6 times faster PCA when compared to the ZnO–TiO_2 CSHJ because of efficient *hole* capture by oxygen vacancies, and the lower mobility of *holes*.

Introduction

Heterostructure catalysts for the oxidative degradation of environmental pollutants or chemical conversions are well known for their efficiency where the photo-generated charge carriers are driven apart before recombination.[1–11] Understanding the catalysis mechanism is vital for the design of new functional materials to be a part of an environmentally friendly technology. The catalytic process on the surface of a semiconductor has been proposed by Izumi *et al.*[12] and Matthews.[13] To begin the process of catalysis, the formation of the hydroxyl radical is crucial, which is feasible through (a) *electrons* and/or (b) *holes*. Izumi *et al.*[12] suggested that the processes (a) and (b) are both possible, while Matthews[13] proposed only the process (b). The design strategy requires that the new generation catalysts should prolong the lifetime of the photo-generated charge carriers to elevate their participation in photocatalytic activity (PCA). For such designs, use of heterostructures is an ideal option, where an electron reservoir from a noble metal[2,7–9] or another semiconductor (heterojunction)[5,14,15] is brought into contact. The former case is exploited in core–shell[7,8,11] and nanocomposite[2,9,10] formats, in which the photo-*electrons* from the conduction band (CB) of the semiconductor are transferred to the noble metal and then to the catalysis process, while the *holes* react from the valance band (VB) of the semiconductor. In the latter case, photo-generated *e*/*h* pairs diffuse across the heterojunction and *electron* and/or *hole* take part in the catalysis from CB and VB of each semiconductor, respectively.[4–6] For example, in the ZnO/ZnSe (ref. 5) heterojunction, the PCA takes place at the VB of ZnSe and CB of ZnO. It is notable that most studies on this topic aim to enhance the PCA, while on the other hand understanding the roles of the *electron* and *hole* is equally important to design the new generation catalysts.

In all the above cases, both the charge carriers (*electron* and *hole*) are involved in catalysis, which makes it rather hard to determine unambiguously the individual role of each, apart from in the intrinsic surface chemistry[16] of the materials. However, it is notable that the charge exchange process and hence the mechanism of PCA at heterojunction is still unclear

[a]*UNAM-National Nanotechnology Research Centre, Bilkent University, Ankara, 06800, Turkey. E-mail: svempati01@qub.ac.uk; uyar@unam.bilkent.edu.tr*

[b]*Institute of Materials Science & Nanotechnology, Bilkent University, Ankara, 06800, Turkey*

† Electronic supplementary information (ESI) available: Additional SEM image of the CSHJ, XPS spectra and mechanism demonstrating PCA at the surface of pure TiO_2. See DOI: 10.1039/c3nr06665g

even after the decades of research.[17] Nevertheless, if one of the charge carriers can be effectively isolated from the catalysis then this would offer useful insights for future studies on the design of new catalytic materials. In this direction, we have exploited the fundamental behavior of photo-generated charge carriers in semiconductor heterojunctions, and fabricated 'core–shell' nanofibers where only one of the semiconductors participates in the PCA, while the counter semiconductor allows the diffusion of either an *electron* or *hole* depending on the band alignment. For such a combination, we have considered two potential materials which have attracted a lot of attention in PCA (*i.e.* TiO_2 (ref. 3, 4 and 6–8) and ZnO (ref. 9–11 and 18–23)) and fabricated ZnO–TiO_2 and TiO_2–ZnO as core–shell nanofibers, respectively. To be more precise, the present design enabled the selectivity of either *electrons* or *holes* at the TiO_2 or ZnO surfaces, respectively. These core–shell heterojunction (CSHJ) nanofibers were fabricated at the nanoscale *via* combining electrospinning and atomic layer deposition (ALD). It is notable that similar structures were studied, however, for their O_2 (ref. 24 and 25) and NO_2 (ref. 25) sensing characteristics. In an earlier article by Agrawal *et al.*,[26] spherical core–shell structures were studied only in one combination (ZnO–TiO_2) for their PCA. Pd@CeO_2 hollow core–shell catalysts were studied for photo as well as thermal catalysis.[2] In both cases,[2,26] however, the charge carrier separation and their individual roles were not addressed. Recently, an interesting study appeared in literature in which photo-generated *e*/*h* pairs from a $[Ru(bpy(CO_2CH_3)_2)_3]^{2+}$ based visible-light-sensitizer were separated *via* Co_3O_4–SiO_2 core–shell nanoparticles.[1] The separated *holes* are migrated through the SiO_2 shell into the Co_3O_4 core and the *electrons* directly participate in the catalysis. Other investigations on core–shell structures include $PbTiO_3$–TiO_2,[27] (Ba,Sr)TiO_3–TiO_2 (ref. 28) *etc.* These studies emphasize the need for a better understanding of the roles of the *electron* and *hole* in the catalysis. In the present case the CSHJs were structurally well characterized and their optical properties were studied in conjunction with intrinsic defects where it is generally accepted that the oxygen vacancies (V_Os) influence the PCA. Structurally, the case with TiO_2 is interesting where the phase dependent band gap has shown its effects on the PCA.[3,29,30] By considering this, a single (anatase) phase material was synthesized to reduce the complexity of the analysis, which enabled the precise determination of the individual role of each photo-generated charge carrier in the PCA.

Experimental section

Materials

Poly(vinylpyrrolidone) (PVP, M_w ~1.3 × 10^6, Sigma-Aldrich), titanium(IV)isopropoxide (TTIP, 97%, Sigma-Aldrich), zinc acetate dihydrate (ZnAc, reagent grade, Sigma-Aldrich), ethanol (≥99.8%, Sigma-Aldrich), glacial acetic acid (100%, Merck) and *N*,*N*-dimethylformamide (DMF, Pestanal, Riedel) were used in electrospinning. Tetrakis(dimethylamido)titanium (TDMAT, Sigma-Aldrich), diethylzinc (DEZn, Sigma-Aldrich), and HPLC grade water (H_2O) were used in the ALD processes. Methylene blue (MB, Sigma-Aldrich, certified by the Biological Stain Commission) was used as a model organic dye to evaluate the PCA of the ZnO–TiO_2 and TiO_2–ZnO CSHJ nanofibers. Deionized (DI) water is obtained from a Millipore MilliQ system. All the chemicals were used as received.

Electrospinning of PVP–ZnAc and PVP–TTIP nanofibers

PVP–ZnAc solution. PVP (0.4 g) was dissolved in an ethanol (2 mL)/DMF (2 mL) solvent mixture for 1 h. Then 1.4 g ZnAc was added to this PVP solution and stirred for 2 h to yield a homogeneous PVP–ZnAc solution.

PVP–TTIP solution. TTIP (2.88 mL) was stirred in a glacial acetic acid (2 mL)/ethanol (2 mL) solvent system for 15 min, and PVP (0.6 g) solution in ethanol (3 mL) was added to the above. The resulting mixture was constantly stirred for 2 h, and the yellowish PVP–TTIP solution was obtained.

The above two precursor solutions were taken into two separate syringes fitted with metallic needle (~0.6 mm of inner diameter). Each of the syringes was placed horizontally on a syringe pump (KD Scientific, KDS 101). An electric field of ~15 kV (Spellman, SL Series) was applied across the syringe needle and stationary metal collector (covered with a clean aluminum foil). The tip to collector distance was between 10 and 12 cm. Electrospinning was carried out in an enclosed chamber at ~25 °C and 10% relative humidity. Then an ALD process was implemented on these electrospun PVP–ZnAc and PVP–TTIP nanofibers to yield TiO_2 and ZnO shell structures, respectively.

Atomic layer deposition of TiO_2 and ZnO

TiO_2 and ZnO depositions on the electrospun PVP–ZnAc and PVP–TTIP nanofibers, respectively, were carried out at ~200 °C in a Savannah S100 ALD reactor (Cambridge Nanotech Inc.). N_2 was used as a carrier gas at a flow rate of ~20 sccm. 500 cycles TiO_2 and 144 cycles ZnO were applied using the exposure mode (a trademark of Ultratech/Cambridge Nanotech Inc.) where the dynamic vacuum was switched to static vacuum before each precursor pulse by closing the valve between the reaction chamber and the pump, and switched back to dynamic vacuum for purging excess precursor molecules and gaseous by-products. This allows the substrate to be exposed to precursor molecules for a certain amount of time (*i.e.* exposure time). For the TiO_2 deposition, one ALD cycle was as follows: valve OFF/N_2 flow set to 10 sccm/TDMAT pulse (0.1 s, TDMAT heated to ~75 °C)/exposure (10 s)/valve ON/N_2 purge (20 sccm, 10 s)/valve OFF/N_2 flow set to 10 sccm/H_2O pulse (0.015 s)/exposure (10 s)/valve ON/N_2 purge (20 sccm, 10 s). For the ZnO deposition, one ALD cycle consists of the following steps: valve OFF/N_2 flow set to 10 sccm/H_2O pulse (0.015 s)/exposure (10 s)/valve ON/N_2 purge (20 sccm, 10 s)/valve OFF/N_2 flow set to 10 sccm/DEZn pulse (0.015 s)/exposure (10 s)/valve ON/N_2 purge (20 sccm, 10 s).

ZnO–TiO_2 and TiO_2–ZnO core–shell heterojunction nanofibers

TiO_2 coated PVP–ZnAc (PVP–ZnAc–TiO_2) and ZnO coated PVP–TTIP (PVP–TTIP–ZnO) nanofibers were calcined at ~500 °C for 3 h in order to remove polymeric precursors. This process

enabled the formation of inorganic cores in both cases, yielding the final CSHJ structures to be ZnO–TiO_2 and TiO_2–ZnO.

Characterization techniques

A scanning electron microscope (SEM, FEI – Quanta 200 FEG) was employed to investigate the morphology and dimensions of the nanofibers before and after the calcination. A nominal 5 nm Au/Pd was sputtered on the samples prior to the observation under SEM. About 100 measurements were considered to determine the average fiber diameter (AFD) from the SEM images. CSHJ nanofibers were subjected to transmission electron microscopy (TEM, FEI-Tecnai G2 F30) where the sample was dispersed in ethanol and a tiny droplet was analyzed from a holey carbon coated TEM grid. TEM-EDX spectra were also recorded for both of the samples. X-ray diffraction (XRD) patterns were recorded in the range of $2\theta = 10$–100° using PANalytical X'Pert Pro Multi Purpose X-ray diffractometer with Cu K_α radiation ($\lambda = 1.5418$ Å). The bonding states of the constituent elements at the surface of the samples (400 μm spot size) were investigated by X-ray photoelectron spectroscopy (XPS, Thermoscientific K-Alpha, Al K_α radiation, $h\nu = 1486.6$ eV) with a flood gun charge neutralizer. For the core-level spectra, the pass energy and step size were set to 30 eV and 0.1 eV, respectively. VB spectra were also recorded with a pass energy of 30 eV in energy steps of 0.2 eV. Spectral deconvolutions of the XPS data were performed through the Avantage software. A Horiba Scientific FL-1057 TCSPC was used for the photoluminescence (PL) measurements performed at an excitation wavelength of ~360 nm.

Photocatalytic activity of core–shell heterojunction nanofibers

The photo-induced degradation efficiency of the CSHJ samples (~5.7 mg each) was analyzed by immersing them individually into quartz cuvettes containing MB aqueous solution (0.25 mM). The cuvettes were placed at a distance of ~10 cm from the UV source (8 W, UVLMS-38 EL) operating at a wavelength of 365 nm. Dye concentrations in the cuvettes were measured using a UV-Vis-NIR spectrophotometer (Varian Cary 5000) at regular time intervals. Each CSHJ sample was immersed down at the bottom of the cuvette during the UV-Vis measurement and therefore did not interfere with the data acquisition.

Results and discussion

Fig. 1 is a schematic diagram depicting the fabrication of the CSHJ nanofibers, where the various processes and sequence of the steps are described. ZnO–TiO_2 and TiO_2–ZnO CSHJs were fabricated *via* a three-step process where electrospinning was followed by atomic layer deposition (ALD) and calcination. In the first step, we prepared precursors *via* electrospinning[31–34] for the cores of the CSHJ nanofibers, where the precursors were mixtures of PVP and ZnAc or TTIP. In the second step, these nanofibers were used as substrates and TiO_2 or ZnO shell was grown through ALD. Finally, the nanofibers were calcined where the organic component (PVP) is removed to form ZnO or TiO_2 in the core of the CSHJs. The adopted calcination temperature and duration yielded single phase and high quality samples.

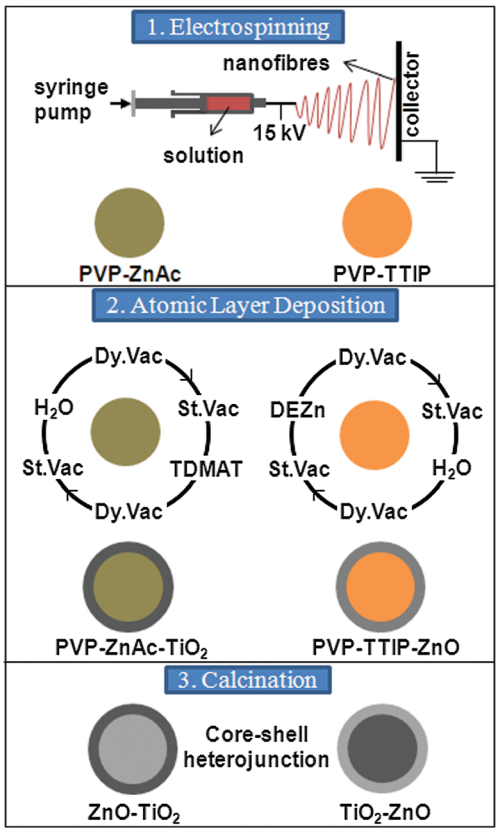

Fig. 1 Schematic diagram depicting the fabrication of core–shell structured heterojunction nanofibers. Dy.Vac and St.Vac stand for dynamic and static vacuum conditions, respectively.

In any ALD process, it is important to consider the compatibility between the precursor and polymer as the former can degrade the latter by chemically reacting with it; see the case with the ALD of Al_2O_3 on a nylon-6 polymer.[35] On the other hand, in the case of poly(propylene) fibers, an Al_2O_3 base layer is employed to deposit ZnO, where the former protects the diffusion of DEZn into the polymer.[36] Apart from these limitations ALD in fact can yield coral,[37] core–shell[38] like complex nanostructures, which are potential materials for photocatalytic applications.[23,39] Hence we applied this technique in combination with electrospinning to produce core–shell structured nano-entities.

The SEM images of the nanofibers before and after calcination are depicted in Fig. 2. Prior to the calcination and after the ALD process, the AFD are 320 ± 120 and 600 ± 340 nm for PVP–ZnAc–TiO_2 and PVP–TTIP–ZnO nanofibers, respectively (Fig. 2a and b). It is generally accepted that electrospun polymer fibers do possess wide range of diameters, while a rough surface occurs for certain polymers in electrospinning depending upon the solvent and its characteristics.[31–34] After the calcination, the structural integrity of the nanofibers was preserved, while we note a decrease in the AFD values which is expected due to the decomposition and removal of PVP. The final CSHJs, ZnO–TiO_2 and TiO_2–ZnO, have diameters in the range of 100–650 nm and

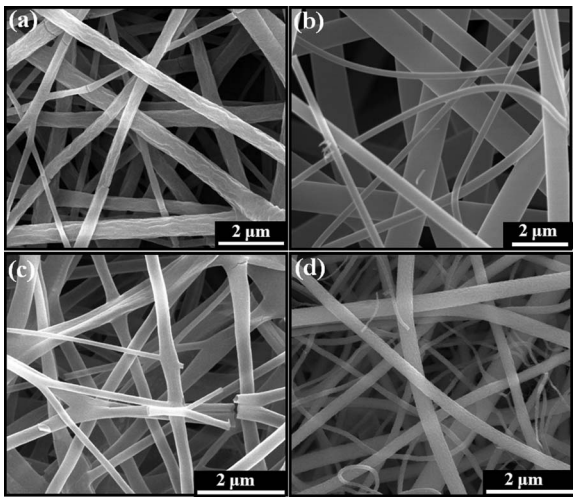

Fig. 2 Representative SEM images of (a) PVP–ZnAc–TiO_2, (b) PVP–TTIP–ZnO, (c) ZnO–TiO_2 and (d) TiO_2–ZnO core–shell heterojunction nanofibers.

50–740 nm with AFD of 270 ± 110 nm and 200 ± 120 nm respectively (Fig. 2c and d). If we compare the AFD before and after calcination, the differences across ZnO–TiO_2 and TiO_2–ZnO can be attributed to the varying PVP content. In the present case the morphological appearances and changes after the calcination are similar to earlier observations.[18,19,33] After calcination CSHJ nanofibers show a rough surface, see Fig. S1 of the ESI.† We will see the similarity in the next section, where the samples were analyzed under TEM.

The CSHJ samples were subjected to TEM characterization (Fig. 3). The core–shell structure can be seen clearly for both of the samples (Fig. 3a and b), where uniformities of the TiO_2 and ZnO shell layers should be pointed out, despite the relatively large surface area of the nanofibers. We have measured the thickness of the shell from these TEM images yielding ~50 nm and ~70 nm for TiO_2 and ZnO, respectively. Furthermore, the grainy structure of shell is explicit from the TEM images, which has been shown to possess single crystallinity as evidenced by the high resolution images (Fig. 3c and d). The interplanar distances were measured for the shell regions, and the values match with the literature. We have annotated these values on Fig. 3c and d for TiO_2 and ZnO, respectively.[40–42] We have also recorded EDX on CSHJs from TEM and the results are given in S2 of the ESI.† For both the cases a signal from Zn and Ti is seen as expected, however, the signal from the shell region dominates. From these spectra, the presence of Ti and Zn is confirmed. The quantification of the elements occurring in the spectra are not given as the signal level from the 'core' part of the structure depends on the characteristics of 'shell' material as the latter encloses the former completely.

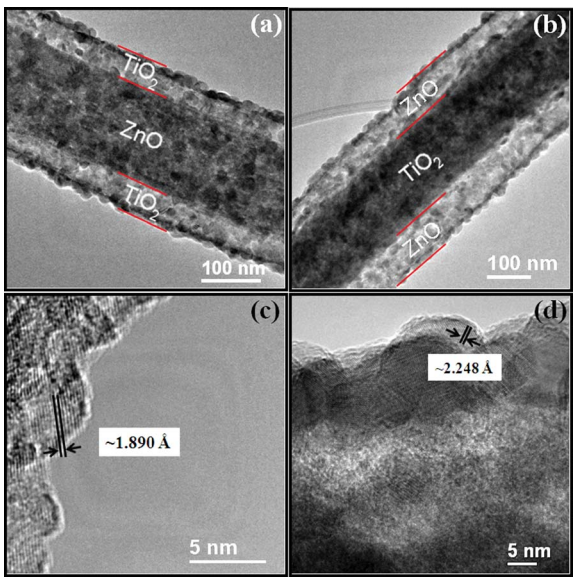

Fig. 3 Representative TEM images of the core–shell heterojunction nanofibers (a) ZnO–TiO_2, (b) TiO_2–ZnO; (c) and (d) HRTEM images of the 'shell' regions of (a) and (b), respectively.

The crystalline phase of TiO_2 should be identified as precisely as possible, given the type II band alignment (band gaps of rutile and anatase are 3.03 eV and 3.20 eV, respectively) and its influence on PCA.[29,30] Importantly given the penetration depth of X-rays, the XRD data contain ZnO and TiO_2 characteristic peaks in both of the heterojunction nanofibers. A list containing the peak positions and the corresponding Miller indices, (*hkl*), for the three cases (anatase TiO_2, rutile TiO_2 and ZnO) has been tabulated in S3 of the ESI.† The XRD pattern relevant to TiO_2 will be discussed for the ZnO–TiO_2 CSHJ (Fig. 4a). We have annotated the Miller indices for the anatase and rutile phases of TiO_2 on Fig. 4a and the peaks corresponding to ZnO are identified on Fig. 4b for brevity. For example (010), (002) and (011) reflections of ZnO can be seen in Fig 4a, indicated by arrows. Furthermore, the diffraction pattern on a log scale (not shown here) was scrutinized for shape changes and asymmetries. A careful inspection of the peak positions (S3 of the ESI†) and the data (Fig. 4a) suggest that the pattern matches well with the anatase phase polycrystalline TiO_2 within the detection limits of XRD. An investigation on

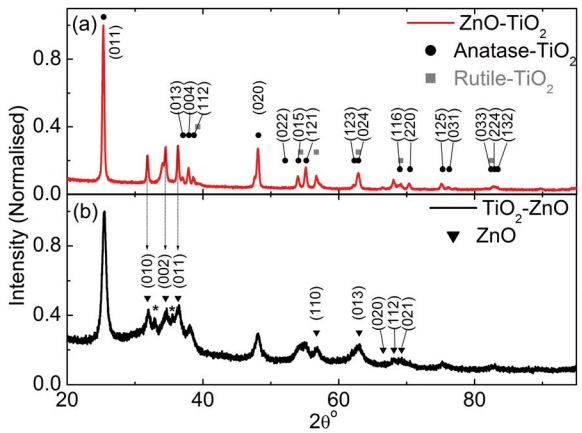

Fig. 4 XRD patterns of core–shell heterojunction nanofibers within the 2θ range of 20–100° (a) ZnO–TiO_2 and (b) TiO_2–ZnO. Standard reflections for TiO_2 (anatase & rutile) and ZnO are annotated. '*' represents the peaks from aluminium oxide.

pure TiO_2 nanofibers (results not shown here) confirmed the formation of an anatase phase (*i.e.* without the ZnO shell, subjected to the same thermal treatments). The peaks in the diffraction pattern are consistent with the literature.[43,44] The lattice parameters were calculated for tetragonal TiO_2 ($a = b =$ 3.7847 Å, and c = 9.5173 Å) and yielded a crystal volume of 136.33 Å^3, which is comparable to the standard value of 135.25 Å^3.[43] However, in the literature lattice contraction is evidenced under the influence of V_Os.[45] In the case of TiO_2 when an O atom is removed, the three nearest Ti atoms tend to relax away from the vacancy in the process of strengthening their bonding with the rest of the lattice.[45,46] In the present case, most probably because of the low density of V_Os, a negligible effect on the bond lengths/cell volume is seen. Moving onto the XRD pattern of the TiO_2–ZnO CSHJ sample, we have identified reflections of the hexagonal (wurtzite) ZnO and annotated the corresponding Miller indices on Fig. 4b. Note that it contains peaks from anatase TiO_2 which were not annotated on Fig. 4b. The XRD pattern indicated a polycrystalline ZnO which was found to be consistent with the literature.[40,41,43,47] The lattice parameters were derived and the c/a ratio of ~1.6 further supports the wurtzite structure and successful formation of ZnO. Since we have collected the nanofibers on Al foil and calcined them after the ALD process, a background of aluminum oxide is evidenced in the TiO_2–ZnO CSHJ (designated with '*' on Fig. 4b).

The surface characterization of the semiconductors such as ZnO[40,41,47] and TiO_2 (ref. 48 and 49) is of prime importance not only in the context of PL but also in conjunction with the PCA. Interestingly, both of these properties are dependent on the ionic state of the chemisorbed surface oxygen,[40,41,47–51] which can be realized precisely with XPS. Note that the physisorbed oxygen can be desorbed under ultra high vacuum conditions. CSHJ samples were subjected to XPS analysis for Ti 2p or Zn 2p, O 1s and the VB. The spectral locations of the deconvoluted peaks are annotated on the image for each of the spectra. A Ti 2p core-level spectrum obtained from ZnO–TiO_2 CSHJ is shown in Fig. S4a of the ESI.† The spectral locations of the peaks corresponding to Ti $2p_{3/2}$ and Ti $2p_{1/2}$ are consistent with the literature and the expected spin-orbit splitting of 5.7 eV is observed.[52] It is also notable that we have not noticed any signatures of Ti^{4+} or Ti^{3+} in the Ti 2p spectrum. The core-level spectrum of Zn 2p from the ZnO–TiO_2 CSHJ is shown in Fig. S4b of the ESI† and the peaks $2p_{3/2}$ and $2p_{1/2}$ indicated a wurtzite structured ZnO where the spin orbit splitting and satellite peak are consistent with the literature.[40,52]

In the context of the core-level spectrum of O 1s from TiO_2 (ZnO–TiO_2 CSHJ), a major peak centered at ~530.4 eV and a minor peak at ~532.2 eV can be seen which correspond to the oxygen[52] in TiO_2 and chemisorbed oxygen, respectively (Fig. 5). The presence of oxygen species such as –OH, –CO, adsorbed H_2O and/or O_2 on the surface generally produces a peak at 532.3 eV.[53–55] Similar to the earlier case, the O 1s spectrum of ZnO (TiO_2–ZnO CSHJ) can be deconvoluted into two peaks as shown in Fig. 5. The spectrum obtained from the ZnO 'shell' has shown a major peak centered at ~530.5 eV corresponding to the oxygen in zinc oxide, which is in line with the literature.[52] The

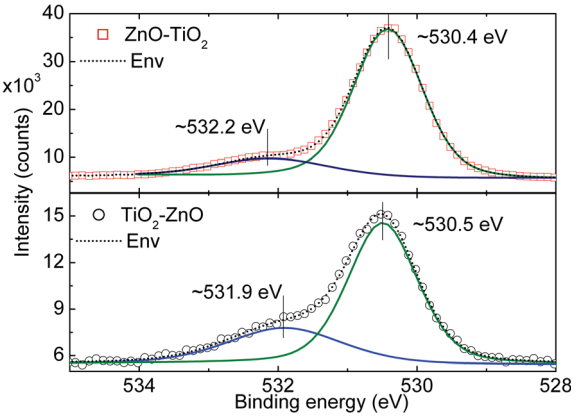

Fig. 5 Core-level XPS spectra of O 1s from the ZnO–TiO_2 and TiO_2–ZnO core–shell heterojunction nanofibers with peak deconvolution. The spectral locations of the peaks are annotated on the image, where the major peak corresponds to the oxygen in the shell material and the minor peak to chemisorbed oxygen.

other minor peak appearing at ~531.9 eV corresponds to the chemisorbed oxygen at the lattice defect sites. The peak at 531.5 eV is attributed to O^- and O^{2-} ions in the oxygen deficient regions on the surface.[53–55]

Due to the fact that TiO_2 and ZnO possess typical oxygen related defects, the defect sites are subjected to the chemisorption of the above ions while sharing the lattice *electron(s)*.[53–55] Furthermore, the grain boundaries (as seen in the TEM images) are obvious locations for electron deficient species to chemisorb. Depending on the availability of free *electron(s)*, the sharing can be partial with the above species which has produced relatively broad binding energies peaking at ~532.2 eV or ~531.9 eV. Among these two samples, it can be seen that the chemisorbed oxygen related to the ZnO–TiO_2 sample shows relatively higher binding energy, obviously because of the differences in the origin of the chemisorbed oxygen. While keeping these differences aside, a variation in the relative area of peaks is demonstrated, where TiO_2–ZnO CSHJ has shown nearly 2.6 times higher area than its complimentary CSHJ. This confirms that a larger fraction of oxygen-defect regions is present in the surface layer[53,55] for TiO_2–ZnO compared to ZnO–TiO_2.

Furthermore, VB spectra (Fig. S5 of the ESI†) of both CSHJs were investigated for any alterations in the edge of the band corresponding to the 'shell' semiconductor. The VB edges were at ~2.35 eV and ~2.42 eV for ZnO–TiO_2 and TiO_2–ZnO, respectively. By the given TiO_2-anatase phase band gap of 3.20 eV, the CB edge should be placed around −0.85 eV. It is notable that the VB edges were found to be in the range of 2.4–3.1 eV with band gaps within the range of 3.67–3.2 eV.[56–58] In the case of ZnO, the CB edge was found to be around −0.88 eV according to its typical band gap of 3.3 eV.

A number of studies[7,8,16,44,48,49,59] have already shown the importance of the lattice defects in conjunction with PCA either in the case of pristine or heterojunction catalysts, where they can be identified through optical properties. We have performed PL spectroscopy on the CSHJ nanofibers (Fig. 6) and the

origin of defect-related emission is overlaid on the corresponding spectrum. When CSHJs were illuminated with energies higher than their band gaps, the majority of the absorption takes place within the 'shell' region. Hence the emission from the CSHJs is mainly due to the shell region of the heterojunctions, where the visible emission occurs from the surface recombination.[41,60,61] In both the cases, a largely similar visible emission indicates a dominant defect density such as V_Os. Importantly, despite the visible emission peaks appearing at almost the same wavelength for both the CSHJs, the energetic location of the V_Os for TiO_2 and ZnO are not the same. These spectra will be discussed independently with reference to the plausible defects in the following sections and subsequently juxtaposed with the PCA. Although the majority of the emission is from the 'shell', it should be noted that the emission and its intensity are influenced by the presence of the 'core' where there might be a recombination route (radiative/non-radiative) for the photo-generated charge.

In the case of the ZnO–TiO_2 sample, the emission from the interband transition is seen at ~3.2 eV. This band arises due to the *e*/*h* recombination across the band gap of TiO_2, while the broad visible emission centered at ~2.4 eV is due to the surface recombination associated with V_Os defects.[44,49] XPS has indicated that there is chemisorbed oxygen on the surface of the CSHJ which further supports the defects related to oxygen vacancies. The energetic locations of these defects are discussed in the literature,[44,49] which were schematized on the emission spectrum (Fig. 6). The *electrons* in V_Os (also known as F centers) are localized because of Madelung potential of the highly ionic crystal.[63] This state can be occupied by O^{2-} by capturing one or two 'free' *electrons* from the crystal, and hence the energetic cost of the vacancy is minimized.[63] These localized *electrons* form a donor level 0.75–1.18 eV below the CB of TiO_2,[44,62] specifically the donor level at 1.18 eV below the CB is due to V_O^{++}.[49] Furthermore, the band arising because of V_Os can be broad enough to merge with the CB in the case of sufficiently highly defective TiO_2 of either the anatase or rutile phase,[64] and hence a significant shift in Fermi level toward high energies can be expected. We believe that this has not happened in the present case where an explicit peak corresponds to the interband transition from TiO_2 and there is a relatively low concentration of V_Os (as evidenced in XPS measurements). On the other hand, the V_Os can cause the redistribution of excess charge among the nearest neighboring Ti atoms ($Ti^{4+}/V_O \rightarrow Ti^{3+}$ or Ti^{2+}) which form a shallow donor state below the CB.[65,66] However in the core-level XPS analysis of the Ti 2p spectrum (Fig. S4a of the ESI†) no explicit indication of these ionic states is present, as mentioned previously.

In the case of TiO_2–ZnO, the emission spectrum from ZnO consists of the least controversial UV-emission (interband transition) which occurred at ~3.2 eV and debatable visible emission centered at ~2.5 eV. Interestingly, the visible emission is attributed to the V_Os, similar to the TiO_2 case. However, this green emission consists of two transitions as depicted in Fig. 6. The V_Os exist in the bulk grain region (BGR)[60] as well as depletion region (DR)[61] with different ionic states. In the BGR, V_O^+ captures an *electron* from CB and forms V_O* 0.86 eV below the CB and in DR, V_O^+ captures a *hole* from VB and forms V_O^{++} 1.16 eV above the VB. While the energetic locations of V_O in TiO_2 range from 0.75 eV to 1.18 eV below the CB,[44,62] however, notably V_O^{++} is 1.18 eV below the CB.[44,49] In the context of TiO_2–ZnO, the BGR of ZnO is not accessible to the PCA, hence only the DR, which is on the surface of the CSHJ, takes part in the PCA by capturing a *hole* from the VB. The optical quality can be compared across the CSHJ by taking the intensity ratios of the interband transition to the visible (I_{UV}/I_{Vis})[40,47] yielding ~0.3 for TiO_2 and ~0.5 for ZnO for ZnO–TiO_2 and TiO_2–ZnO CSHJs, respectively. These ratios suggest that the optical quality of ZnO is better than TiO_2.

In the case of TiO_2, various chemical species (–OH, –CO, H_2O or O_2) were found to be chemisorbed on the surface which are not the same as in the ZnO case (O^- and O^{2-}). Although the species adsorbed on either of the surfaces were not exactly identified, it is clear that for TiO_2 chemisorption occurred at a higher energy than ZnO. *i.e.* the surface adsorbents of TiO_2 bind to the lattice more strongly than those of ZnO, which explains the differences in the relative intensities of visible emission among TiO_2 and ZnO. In the case of TiO_2, since the surface adsorbents are strongly bound to the lattice they can successfully capture an *electron* from the CB and give rise to visible emission. In contrast, for the case of ZnO, despite their relatively high density, the surface adsorbents are loosely bound and hence under equilibrium, they have relatively lower probability to stay at the defect site and thus to give visible emission.

Furthermore, we would like to comment on the visible emission from the CSHJ. Within the interfacial region between the semiconductors, there is a certain possibility of so called 'interfacial states' which may arise due to the lattice mismatch or other related effects. These states can be radiative or non-radiative in nature, which can enhance or subdue the visible-intensity,

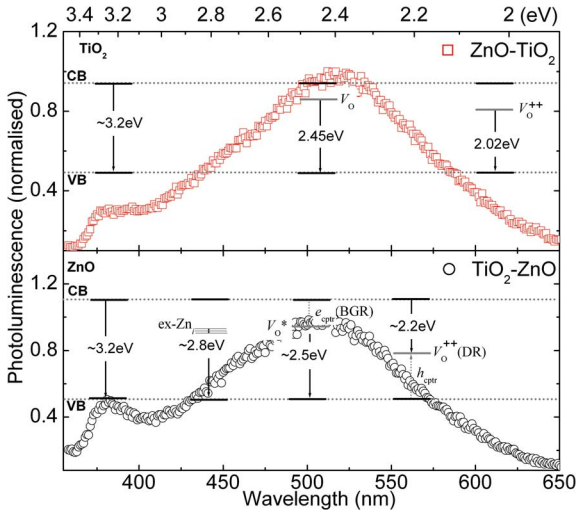

Fig. 6 Photoluminescence spectra of ZnO–TiO_2 and TiO_2–ZnO core–shell heterojunction nanofibers. The defects and related emission from the 'shell' region are schematized on the image. In the bulk grain region (BGR)[60] and in the depletion region (DR)[61] $V_O^+ \rightarrow V_O$* (0.86 eV below the CB) and $V_O^+ \rightarrow V_O^{++}$ (1.16 eV above the VB) processes take place, respectively. V_Os in TiO_2 are 0.75–1.18 eV below the CB,[44,62] while V_O^{++} in TiO_2 is 1.18 eV below the CB.[44,49]

respectively. We have not considered the possible emission from the interface, as the oxide hetero-interfaces are not completely understood yet.[17] Nevertheless, the present design enables future studies to identify the role of each charge-carrier for oxidation processes of various organic compounds, see ref. 50 and 72–81 in ref. 16 and the recent study as well.[1]

Having discussed the influence of defects on the optical properties, the involvement and role of V_Os in the interface of heterojunctions is still debatable,[48] on the other hand since no catalysis takes place at the interface, the dynamics and consequent charge exchange process are out of the scope of the present article. Essentially if V_Os in TiO_2 exist inside the lattice then they may serve as recombination centers, however this may reduce the PCA.[67] In a recent article, the importance of oxygen vacancies in TiO_2 and their influence on the PCA has been emphasized.[48] Prior to the discussion on PCA, it should be noted that no charge carrier is excited to the defect states directly as we have employed a monochromatic UV source (365 nm) and hence the defect sites can capture *electrons* or *holes* depending on their energetic location within the band gap.

It is useful to revisit the photocatalysis mechanism[12,13] to which we will be referring in the context of PCA for each CSHJ. This process is shown as follows after Izumi *et al.*[12] and Matthews.[13] The key for the photocatalysis is the formation of the hydroxyl radical ($^{\bullet}OH$), which can be through (a) an *electron* generated at the CB (e^-_{CB}) and/or (b) a *hole* generated at the VB (h^+_{VB}). Process (a) contains multiple steps (see below), which are mediated by superoxide anions ($^{\bullet}O_2^-$) as proposed by Izumi *et al.*[12] Initially, molecular oxygen traps the e^-_{CB} and forms $^{\bullet}O_2^-$ ions (a1-1), while the second step involves formation of H_2O_2 ((a2-1) through (a2-4)) followed by its cleavage by superoxide anions ((a3-1), (2) or (3)) as shown below.

$$e^-_{CB} + O_2 \rightarrow {}^{\bullet}O_2^- \quad \text{(a1-1)}$$

$$^{\bullet}O_2^- + H^+ \rightarrow {}^{\bullet}HO_2 \quad \text{(a2-1)}$$

$$2{}^{\bullet}HO_2 \rightarrow H_2O_2 + O_2 \quad \text{(a2-2)}$$

$$^{\bullet}O_2^- + {}^{\bullet}HO_2 \rightarrow {}^{\bullet}HO_2^- + O_2 \quad \text{(a2-3)}$$

$$^{\bullet}HO_2^- + H^+ \rightarrow H_2O_2 \quad \text{(a2-4)}$$

$$H_2O_2 + {}^{\bullet}O_2^- \rightarrow {}^{\bullet}OH + OH^- + O_2 \quad \text{(a3-1)}$$

(or)

$$H_2O_2 + e^-_{CB} \rightarrow {}^{\bullet}OH + OH^- \quad \text{(a3-2)}$$

(or)

$$H_2O_2 \xrightarrow{h\nu} 2{}^{\bullet}OH \quad \text{(a3-3)}$$

On the other hand, in process (b),[13] $^{\bullet}OH$ radicals are formed mainly from the h^+_{VB} in the presence of either adsorbed H_2O (b-1) or the OH^- groups on the surface (b-2).

$$h^+_{VB} + H_2O \rightarrow {}^{\bullet}OH + H^+ \quad \text{(b-1)}$$

$$h^+_{VB} + HO^- \rightarrow {}^{\bullet}OH \quad \text{(b-2)}$$

Finally, in any case the $^{\bullet}OH$ radical oxidizes the dye ($^{\bullet}OH$ + dye → oxidized products) when generated by a photo-*electron* or photo-*hole*.

Moving on to the context of the CSHJ, its functionality depends on fundamental physical parameters such as band offset, where there exists a profound effect on the carrier confinement and electronic transport along and across the interface.[17] Further complicating the process of charge transfer, the oxide hetero-interfaces are not well understood yet.[17] In the present case initial precursor nanofibers of ZnO or TiO_2 were produced, then the counter semiconductor is deposited. This intermediate level heterostructure was subjected to calcination, producing the hetero-oxide interface with a structural distortion along with a probability of chemical bonds and charge distribution across the junction. The present calcination parameters yielded anatase TiO_2 in both of the heterojunctions. On the other hand, it is acknowledged that mixed phase TiO_2 yields a higher PCA;[29,30,68] however, we aim to determine the individual roles of *electrons* and *holes* in the process of catalysis. In the mixed phase TiO_2, the energetic alignment of band edges suggests a flow of conduction *electrons* from rutile to anatase.[30] Keeping this in the background, we chose to produce a single phase TiO_2 to study the catalytic mechanism. On the other hand, defect disorders in either TiO_2 or ZnO play a significant role in the PCA. Hence we refer to the discussion of PL from TiO_2 and ZnO, and correlate it with the PCA of ZnO–TiO_2 and TiO_2–ZnO CSHJ, respectively.

PCA is compared across the CSHJ while considering the degradation of MB without any catalyst (Fig. 7). The photodegradation of chemical compounds on the surface of a semiconductor most often follows[16] Langmuir sorption isotherms,[69] where a single molecule deep monolayer is adsorbed at a distance of ~1 Å. The exponential decay behavior (Fig. 7) suggests pseudo-first-order kinetics according to the Langmuir–

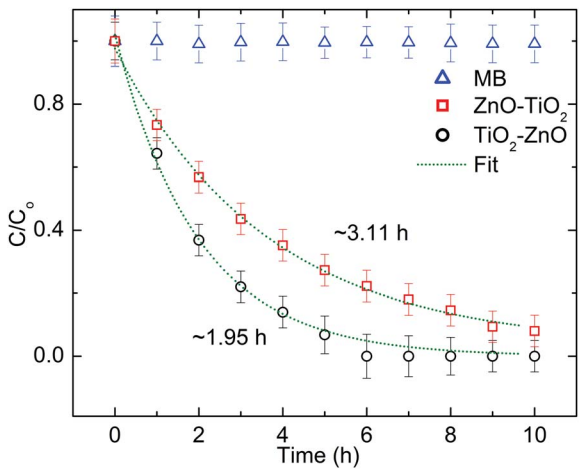

Fig. 7 Photocatalytic activities of the ZnO–TiO_2 and TiO_2–ZnO core–shell heterojunction nanofibers. Exponential decay fits and constants are shown when compared with the pristine methylene blue (MB) without any catalyst.

Hinshelwood model. In any photocatalysis involving a semiconductor, the efficiency of the process depends on the balance between the interfacial charge transfer (semiconductor to dye) and charge carrier recombination lifetime.[16] In the present investigation, the degradation time constants yielded from an exponential fit for each CSHJ are given on Fig. 7. In the absence of a catalyst, MB did not show any degradation at a noticeable level while ZnO–TiO_2 and TiO_2–ZnO CSHJs yielded ~3.11 h and ~1.95 h decay times, respectively. These decay times indicate how fast the catalysts can oxidize the dye which is being tested. Interestingly, the time constant shown by the TiO_2–ZnO CSHJ is nearly 1.6 times faster than that of the ZnO–TiO_2 CSHJ. It is vital to understand the diffusion of *electrons* or *holes* across the CSHJs prior to the explanation of the variation observed in the PCA.

In Fig. 8 we have shown a schematic diagram which replicates the semiconductors with energetic locations with respect to vacuum for both CSHJs. Previously discussed processes are annotated on the figure, *i.e.* (a) and (b) while considering the nature of defect. In the context of ZnO and TiO_2, these defect-related bands are shown to depict improved catalytic activity.[7,8,16,44,48,49,59]

Role of electrons

Under illumination of the ZnO–TiO_2 CSHJ, *electron* and *hole* pairs are created in the TiO_2 shell region. If we consider the alignments of the band as shown in Fig. 8 (left panel), it is clear that the *holes* can be diffused into the core (ZnO), while the *electrons* can participate in the PCA at the CB, or V_O states of TiO_2. However, there is also a possibility that e^-_{CB} can be transferred to V_O* (BGR) and/or V_O^{++} (DR if it exists) states of ZnO

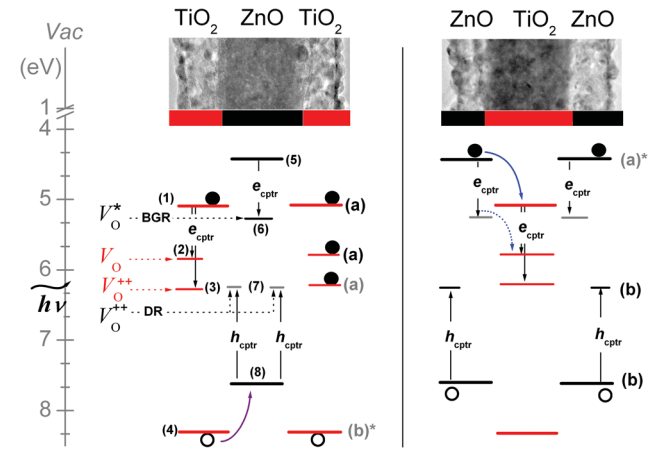

Fig. 8 Proposed catalysis mechanism, where either *electrons* from the TiO_2 or *holes* from the ZnO are engaged from the ZnO–TiO_2 (left panel) and TiO_2–ZnO (right panel) core–shell heterojunction nanofibers. The energetic band locations of TiO_2 were obtained from the references as follows (1),[30] (2),[44,62] (3),[44,49,62] and (4),[30] while for the ZnO case (5),[76] (6),[50,51] (7),[50,51] and (8).[76] The band gaps of TiO_2 and ZnO were taken as 3.2 eV (ref. 30) and 3.3 eV,[76] respectively. The processes (a) and (b) stand for *acceptor* → *acceptor*$^-$ and *donor* → *donor*$^+$, respectively. e_{cptr} and h_{cptr} stand for *electron* and *hole* capture, respectively.

directly or after they have been captured by the V_O states of TiO_2. In the present context, we are discussing the V_Os that are limited to the surface of the TiO_2 and the *electrons* at such defects have almost no mobility to reach the V_O^{++}s or V_O*s of ZnO. Photo-generated *electrons* in the VB of TiO_2 find the V_O* state energetically favorable, however physically not reachable, because V_O* lies in the bulk of the ZnO. Hence the *electron* has to take part in the PCA before the recombination. However the *electrons* in the V_Os of TiO_2 can reach the DR (grain boundaries of ZnO), which might hinder the PCA. Furthermore, if V_Os exist inside the lattice then they may serve as recombination centres.[67] Since the *holes* are most likely diffuse into ZnO, they may not play a major role in the PCA. The above argument assumes that *e*/*h* pairs are not created in ZnO, where TiO_2 absorbs almost all of the UV illumination. However, in the case that they are generated in ZnO dominantly, e^-_{CB} may migrate to the CB of TiO_2 and participate in the PCA. Hence the active sites for the PCA at the TiO_2 surface are CB and V_Os as designated by process (a) on Fig. 8, left panel. In the case of TiO_2, the existence of V_Os creates unpaired *electrons* or Ti^{3+} centres (though not evidenced in the XPS), which could form donor levels[49] and also the *e*/*h* recombination process is affected causing a change in chemical rates.[59] If we look at the mechanism of catalysis for pure TiO_2, under suitable illumination, the photo-generated *electrons* either at the CB or V_Os are captured by O_2, producing O_2^- radical groups where the adsorption energies are −0.94 and −2.52 eV, respectively.[70] As discussed earlier, these radical groups are the key for the oxidation of the test dye. Notably, a high density of V_Os can induce vacancy electronic states below the CB[71] and an improved PCA is noticed under the visible light. Since charge migration is a physical process, it may be possible that some of the *holes*, which are not migrated to the core, can participate in the PCA as indicated with (b)* on Fig. 8, left panel, however with negligible activity. Deconvolution of the visible emission (not shown here) from TiO_2 suggests that the emission from the optical transition from V_O^{++} to the VB has relatively lower intensity when compared to that from V_O (which are 0.75 eV below the CB) to the VB, which implies that the defect density of V_O^{++} is relatively less. Hence the *electron* capture from the CB is dominated by V_O, which is 1.18 eV below the CB,[44,49,62] see left panel of Fig. 8, black coloured (a). Furthermore, similar to the molecular oxygen, H_2O can involve in the PCA when disassociated at a defect site, e.g. V_O (energetically more favourable[72]), while on a perfect TiO_2 surface H_2O is physically adsorbed.[73–75]

Role of holes

In contrast to the previous CSHJ, the present heterojunction favours *electrons* to migrate to the TiO_2-core leaving the *holes* at the VB to participate in the PCA. Otherwise, this photo-generated *electron* can be captured by V_O* which can further diffuse into the TiO_2-core by accessing V_Os therein, as shown in the Fig. 8, right panel. Hence the active *holes* at the surface of the ZnO-shell take part in the PCA and the above-discussed mechanism can be taken into account to understand the oxidation process. Since the surface layer is only ZnO, it has been revealed that V_Os can behave as important adsorption and active sites for

catalysis, which strongly influence the reactivity of metal oxides.[77] Notably, V_O^{++} forms after capturing a *hole* from the VB. Hence by involving H_2O to form $^{\bullet}OH$ the dye is oxidized as shown earlier in eqn (b-1) and (b-2). Similar to the earlier case, it may be possible that some of the *electrons*, which are not migrated to the core, can participate in the PCA. However, the activity with such *electrons* is negligible and shown with grey coloured (a)* on Fig. 8, right panel.

The higher PCA for the TiO_2–ZnO CSHJ can be because of various reasons, including a high density of surface defects and lower binding energy of the surface adsorbents, which can exchange the charge carrier and participate in the PCA. In ZnO, under biased and illuminated conditions,[51] the mobility of the *hole* (10 $cm^2\ V^{-1}\ s^{-1}$) would be much lower when compared to unbiased conditions such as those used here. From the earlier described processes (a) and (b), it is clear that $^{\bullet}OH$ radical forms with O_2 (primary)/*electrons* and/or H_2O/*hole*. In the case of ZnO–TiO_2, *electrons* are the main participants in the PCA, hence the availability of the O_2 can be a limiting factor. On the other hand, for the TiO_2–ZnO CSHJ, the vast availability of H_2O is an advantage to yield higher efficiency. Therefore in the context of an aqueous solution *holes* may yield a higher PCA than *electrons.* In the case of TiO_2, the charge carrier generation under suitable illumination takes place in the order of fs, and subsequent processes such as charge carrier trapping and recombination take place in 0.1–10 ns and 10–100 ns, respectively (Fig. S6 of the ESI†). We can see that trapping is 10 times faster and the trapped charge has to participate in recombination.[16] Also, it is suggested that the *electron* transfer to oxygen may be the rate determining step, see ref. 43, 86 and 87 in Hoffmann *et al.*[16] Depending on the surface chemistry, there is a possibility that there exists more than one type of binding. For example, in the case of $CHCl_3$ interacting with Degussa P25 at pH 5, two different sites of non-uniform binding energies are identified. The stronger binding site dominates sorption at concentrations <1 mM, and the weaker binding state is considered mostly for concentrations >1 mM, see ref. 50 in Hoffmann *et al.*[16] It is thought that high density of defects would lead to a higher PCA; however, this is the case only when we have loosely bound species at the lattice. As in the case of TiO_2, although there are significant defects, they are occupied with strongly bound adsorbents and hence may not be easily brought into the catalysis process where an exchange of charge is required. Although we have not considered the effect of pH, it is notable that water disassociation equilibrium depends on the pH of the solution, which is quite complex in the context of UV-irradiated TiO_2. On the other hand, pH also determines the surface charge of TiO_2 with respect to its point of zero charge (pzc, ~6.5), as well as the ionization state of the organic reactant and of its metabolites.[78] If the pH is higher than the pzc, the surface becomes negatively charged, the opposite is valid for pH < pzc. In the present case, since MB is a cationic dye, the most favorable adsorption occurs at pH < pzc, where the adsorption is the basic requirement[69] for the reaction to take place.[16] We believe that the integral effect of above reasons caused photogenerated *holes* from ZnO to have higher efficiency than *electrons* from TiO_2.

Conclusions

In this study we have attempted to determine the individual roles of *electrons* and *holes* in photocatalysis, which are photo-derived from a core–shell structured semiconducting hetero-junction, where the design enables only the 'shell' part of the CSHJ to be exposed for the PCA. These CSHJs were characterized for their structural integrity, which revealed the formation of pure, single-phase anatase TiO_2 in both CSHJs. TEM analysis suggested well-developed grains, which in principle influence the PCA by forming grain boundaries. XPS has evidenced typical V_Os on the surface hosting various oxygen-related species. The optical properties of the CSHJs were studied and discussed with reference to the intrinsic defects. We have not considered the interfacial defects between core and shell regions, however, the interface is not directly accessible for the PCA anyway. In the case of ZnO the visible emission occurs from the surface, and hence considering the defects limited to the surface does not undermine the analysis. Crucially, under suitable illumination, *e*/*h* pairs are created mainly in the shell region of the CSHJs, and *holes* and *electrons* migrate to the core of the structure for ZnO–TiO_2 and TiO_2–ZnO structures, respectively, as governed by the band alignment.

In the ZnO–TiO_2 CSHJ *e*/*h* pairs are created in TiO_2 and *electrons* take part in catalysis at the CB of TiO_2 while *holes* migrate to the core of the structure. The PCA in this hetero-junction is an integral effect of catalysis taking place at the VB and V_O sites on the surface, where the photo-generated *holes* are eliminated. In the TiO_2–ZnO CSHJ, *e*/*h* pairs are created majorly in ZnO, and *electrons* are diffused into the core while *holes* at the VB of ZnO involve in PCA. The results suggested that TiO_2–ZnO CSHJ has shown higher PCA than the other combination. It might be because of surface chemistry and the intrinsic characteristics of the photo-generated charge carriers. The density of the V_Os for ZnO-shell is higher than TiO_2-shell (XPS), which might have enhanced the *hole* capture process thereby contributing to the PCA. The densities of oxygen related defects differ by a factor of 2.6, causing an improvement of nearly 1.6 times in the PCA. Apparently, this is not linear scaling because of the differences in the chemical nature of the defects. Finally the higher PCA for ZnO shell can be because of high density of defects, lower binding energy of surface adsorbents, and comparatively lower mobility of the *holes* in the VB.

Acknowledgements

S.V. thanks The Scientific & Technological Research Council of Turkey (TUBITAK) (TUBITAK-BIDEB 2216, Research Fellowship Programme for Foreign Citizens) for postdoctoral fellowship. F.K. and C.O.-A. thank TUBITAK-BIDEB for PhD scholarship. N.B. thanks EU FP7-Marie Curie-IRG for funding NEMSmart (PIRG05-GA-2009-249196). T.U. thanks EU FP7-Marie Curie-IRG (NANOWEB, PIRG06-GA-2009-256428) and The Turkish Academy of Sciences – Outstanding Young Scientists Award Program (TUBA-GEBIP) for funding. Authors thank M. Guler for technical support for TEM analysis.

Notes and references

1 A. Agiral, H. S. Soo and H. Frei, *Chem. Mater.*, 2013, **25**, 2264–2273.
2 N. Zhang and Y.-J. Xu, *Chem. Mater.*, 2013, **25**, 1979–1988.
3 H. Y. Zhu, J.-C. Zhao, J. W. Liu, X. Z. Yang and Y. N. Shen, *Chem. Mater.*, 2006, **18**, 3993–4001.
4 L. Liu, X. Gu, C. Sun, H. Li, Y. Deng, F. Gao and L. Dong, *Nanoscale*, 2012, **4**, 6351–6359.
5 S. Cho, J.-W. Jang, J. S. Lee and K.-H. Lee, *Nanoscale*, 2012, **4**, 2066–2071.
6 T. Jiang, T. Xie, L. Chen, Z. Fu and D. Wang, *Nanoscale*, 2013, **5**, 2938–2944.
7 N. Zhang, S. Liu and Y.-J. Xu, *Nanoscale*, 2012, **4**, 2227–2238.
8 H. Tada, T. Kiyonaga and S. Naya, *Chem. Soc. Rev.*, 2009, **38**, 1849–1858.
9 C. Yu, K. Yang, Y. Xie, Q. Fan, J. C. Yu, Q. Shu and C. Wang, *Nanoscale*, 2013, **5**, 2142–2151.
10 Y. Zuo, Y. Qin, C. Jin, Y. Li, D. Shi, Q. Wu and J. Yang, *Nanoscale*, 2013, **5**, 4388–4394.
11 S. Wang, Y. Yu, Y. Zuo, C. Li, J. Yang and C. Lu, *Nanoscale*, 2012, **4**, 5895–5901.
12 I. Izumi, W. W. Dunn, K. O. Wilbourn, F. R. F. Fan and A. J. Bard, *J. Phys. Chem.*, 1980, **84**, 3207–3210.
13 R. W. Matthews, *J. Catal.*, 1986, **97**, 565–568.
14 C. Yu, G. Li, S. Kumar, K. Yang and R. Jin, *Adv. Mater.*, 2013, **26**, 892–898.
15 X. Zong, H. Yan, G. Wu, G. Ma, F. Wen, L. Wang and C. Li, *J. Am. Chem. Soc.*, 2008, **130**, 7176–7177.
16 M. R. Hoffmann, S. T. Martin, W. Choi and D. Bahnemann, *Chem. Rev.*, 1995, **95**, 69–96.
17 H. Seo, A. B. Posadas, C. Mitra, A. V. Kvit, J. Ramdani and A. A. Demkov, *Phys. Rev. B: Condens. Matter Mater. Phys.*, 2012, **86**, 075301.
18 F. Kayaci, C. Ozgit-Akgun, I. Donmez, N. Biyikli and T. Uyar, *ACS Appl. Mater. Interfaces*, 2012, **4**, 6185–6194.
19 F. Kayaci, C. Ozgit-Akgun, N. Biyikli and T. Uyar, *RSC Adv.*, 2013, **3**, 6817–6820.
20 T. J. Athauda, U. Butt and R. R. Ozer, *RSC Adv.*, 2013, **3**, 21431–21438.
21 T. J. Athauda, P. Hari and R. R. Ozer, *ACS Appl. Mater. Interfaces*, 2013, **5**, 6237–6246.
22 T. J. Athauda and R. R. Ozer, *Cryst. Growth Des.*, 2013, **13**, 2680–2686.
23 B. Gong, Q. Peng, J.-S. Na and G. N. Parsons, *Appl. Catal., A*, 2011, **407**, 211–216.
24 J. Y. Park, S.-W. Choi, J.-W. Lee, C. Lee and S. S. Kim, *J. Am. Ceram. Soc.*, 2009, **92**, 2551–2554.
25 S. W. Choi, J. Y. Park and S. S. Kim, *Nanotechnology*, 2009, **20**, 465603.
26 M. Agrawal, S. Gupta, A. Pich, N. E. Zafeiropoulos and M. Stamm, *Chem. Mater.*, 2009, **21**, 5343–5348.
27 L. Li, Y. Zhang, A. M. Schultz, X. Liu, P. A. Salvador and G. S. Rohrer, *Catal. Sci. Technol.*, 2012, **2**, 1945–1952.
28 L. Li, G. S. Rohrer and P. A. Salvador, *J. Am. Ceram. Soc.*, 2012, **95**, 1414–1420.
29 G. H. Li and K. A. Gray, *Chem. Phys.*, 2007, **339**, 173–187.
30 D. O. Scanlon, C. W. Dunnill, J. Buckeridge, S. A. Shevlin, A. J. Logsdail, S. M. Woodley, C. R. A. Catlow, M. J. Powell, R. G. Palgrave, I. P. Parkin, G. W. Watson, T. W. Keal, P. Sherwood, A. Walsh and A. A. Sokol, *Nat. Mater.*, 2013, **12**, 798–801.
31 S. Ramakrishna, K. Fujihara, W. Teo, T. Lim and Z. Ma, *An Introduction to Electrospinning and Nanofibers*, World Scientific Publishing Company, Singapore, 2005.
32 J. H. Wendorff, S. Agarwal and A. Greiner, *Electrospinning: Materials, Processing, and Applications*, Wiley-VCH, Germany, 2012.
33 J. V. Nygaard, T. Uyar, M. Chen, P. Cloetens, P. Kingshott and F. Besenbacher, *Nanoscale*, 2011, **3**, 3594–3597.
34 T. Uyar, R. Havelund, J. Hacaloglu, X. Zhou, F. Besenbacher and P. Kingshott, *Nanotechnology*, 2009, **20**, 125605.
35 C. J. Oldham, B. Gong, J. C. Spagnola, J. S. Jur, K. J. Senecal, T. A. Godfrey and G. N. Parsons, *J. Electrochem. Soc.*, 2011, **158**, D549–D556.
36 W. J. Sweet, J. S. Jur and G. N. Parsons, *J. Appl. Phys.*, 2013, **113**, 194303.
37 P. Heikkilä, T. Hirvikorpi, H. Hilden, J. Sievänen, L. Hyvärinen, A. Harlin and M. Vähä-Nissi, *J. Mater. Sci.*, 2012, **47**, 3607–3612.
38 E. Santala, M. Kemmel, M. Leskela and M. Ritala, *Nanotechnology*, 2009, **20**, 035602.
39 I. M. Szilagyi, E. Santala, M. Heikkila, V. Pore, M. Kemmel, T. Nikitin, G. Teucher, T. Firkala, L. Khriachtchev, M. Rsanen, M. Ritala and M. Leskala, *Chem. Vap. Deposition*, 2013, **19**, 149–155.
40 S. Vempati, A. Shetty, P. Dawson, K. K. Nanda and S. B. Krupanidhi, *Thin Solid Films*, 2012, **524**, 137–143.
41 S. Vempati, J. Mitra and P. Dawson, *Nanoscale Res. Lett.*, 2012, **7**, 470.
42 Y. Masuda, T. Ohji and K. Kato, *Cryst. Growth Des.*, 2010, **10**, 913–922.
43 HighScorePlus-Version-3.0e(3.0.5), PANalytical B. V., 30-02-2012 edn., 2012.
44 I. Nakamura, N. Negishi, S. Kutsuna, T. Ihara, S. Sugihara and K. Takeuchi, *J. Mol. Catal. A: Chem.*, 2000, **161**, 205–212.
45 A. Naldoni, M. Allieta, S. Santangelo, M. Marelli, F. Fabbri, S. Cappelli, C. L. Bianchi, R. Psaro and V. D. Santo, *J. Am. Chem. Soc.*, 2012, **134**, 7600–7603.
46 A. Janotti, J. B. Varley, P. Rinke, N. Umezawa, G. Kresse and C. G. V. d. Walle, *Phys. Rev. B: Condens. Matter Mater. Phys.*, 2010, **81**, 085212.
47 S. Vempati, A. Shetty, P. Dawson, K. Nanda and S. B. Krupanidhi, *J. Cryst. Growth*, 2012, **343**, 7–12.
48 X. Pan, M.-Q. Yang, X. Fu, N. Zhang and Y.-J. Xu, *Nanoscale*, 2013, **5**, 3601–3614.
49 M. K. Nowotny, L. R. Sheppard, T. Bak and J. Nowotny, *J. Phys. Chem. C*, 2008, **112**, 5275–5300.
50 J. D. Ye, S. L. Gu, F. Qin, S. M. Zhu, S. M. Liu, X. Zhou, W. Liu, L. Q. Hu, R. Zhang, Y. Shi and Y. D. Zheng, *Appl. Phys. A: Mater. Sci. Process.*, 2005, **81**, 759–762.

51 S. Vempati, S. Chirakkara, J. Mitra, P. Dawson, K. K. Nanda and S. B. Krupanidhi, *Appl. Phys. Lett.*, 2012, **100**, 162104.
52 A. V. Naumkin, A. K. Vass, S. W. Gaarenstroom and C. J. Powell, U. S. Secretary of Commerce, 2012, vol. NIST Standard Reference Database 20, Version 4.1.
53 M. Chen, X. Wang, Y. Yu, Z. Pei, X. Bai, C. Sun, R. Huang and L. Wen, *Appl. Surf. Sci.*, 2000, **158**, 134–140.
54 A. Stănoiu, C. E. Simion and S. Somăcescu, *Sens. Actuators, B*, 2013, **186**, 687–694.
55 S. A. Ansari, M. M. Khan, S. Kalathil, A. N. Khan, J. Lee and M. H. Cho, *Nanoscale*, 2013, **5**, 9238–9246.
56 G. Xiao, X. Wang, D. Li and X. Fu, *J. Photochem. Photobiol., A*, 2008, **193**, 213–221.
57 Y. Xu and M. A. A. Schoonen, *Am. Mineral.*, 2000, **85**, 543.
58 T. Nishikawa, T. Nakajima and Y. Shinohara, *J. Mol. Struct.*, 2001, **545**, 67–74.
59 J. Wang, P. Liu, X. Fu, Z. Li, W. Han and X. Wang, *Langmuir*, 2008, **25**, 1218–1223.
60 K. Vanheusden, W. L. Warren, C. H. Seager, D. R. Tallant, J. A. Voigt and B. E. Gnade, *J. Appl. Phys.*, 1996, **79**, 7983–7990.
61 A. v. Dijken, E. A. Meulenkamp, D. Vanmaekelbergh and A. Meijerink, *J. Lumin.*, 2000, **90**, 123–128.
62 D. C. Cronemeyer, *Phys. Rev.*, 1959, **113**, 1222–1226.
63 G. Pacchioni, *ChemPhysChem*, 2003, **4**, 1041–1047.
64 G. U. v. Oertzen and A. R. Gerson, *J. Phys. Chem. Solids*, 2007, **68**, 324–330.
65 G. Liu, F. Li, D.-W. Wang, D.-M. Tang, C. Liu, X. Ma, G. Q. Lu and H.-M. Cheng, *Nanotechnology*, 2008, **19**, 025606.
66 N. Serpone, *J. Phys. Chem. B*, 2006, **110**, 24287–24293.
67 F. Zuo, L. Wang, T. Wu, Z. Zhang, D. Borchardt and P. Feng, *J. Am. Chem. Soc.*, 2010, **132**, 11856–11857.
68 L. Zhao, M. Han and J. Lian, *Thin Solid Films*, 2008, **516**, 3394–3398.
69 I. Langmuir, *J. Am. Chem. Soc.*, 1918, **40**, 1361–1403.
70 C. L. Muhich, Y. Zhou, A. M. Holder, A. W. Weimer and C. B. Musgrave, *J. Phys. Chem. C*, 2012, **116**, 10138–10149.
71 I. Justicia, P. Ordejon, G. Canto, J. L. Mozos, J. Fraxedas, G. A. Battiston, R. Gerbasi and A. Figueras, *Adv. Mater.*, 2002, **14**, 1399–1402.
72 R. Schaub, P. Thostrup, N. Lopez, E. Lægsgaard, I. Stensgaard, J. K. Nørskov and F. Besenbacher, *Phys. Rev. Lett.*, 2001, **87**, 266104.
73 M. B. Hugenschmidt, L. Gamble and C. T. Campbell, *Surf. Sci.*, 1994, **302**, 329–340.
74 M. A. Henderson, *Langmuir*, 1996, **12**, 5093–5098.
75 V. A. Gercher and D. F. Cox, *Surf. Sci.*, 1995, **322**, 177–184.
76 L. Ley, R. A. Pollak, F. R. McFeely, S. P. Kowalczyk and D. A. Shirley, *Phys. Rev. B: Condens. Matter Mater. Phys.*, 1974, **9**, 600–621.
77 S. Polarz, J. Strunk, V. Ischenko, M. W. E. v. d. Berg, O. Hinrichsen, M. Muhler and M. Driess, *Angew. Chem., Int. Ed.*, 2006, **45**, 2965–2969.
78 H. Lachheb, E. Puzenat, A. Houas, M. Ksibi, E. Elaloui, C. Guillard and J. M. Herrmann, *Appl. Catal., B*, 2002, **39**, 75–90.